Distinct Activation Mechanisms of CXCR4 and ACKR3 Revealed by Single-Molecule Analysis of their Conformational Landscapes

Christopher T. Schafer[a,1], Raymond F. Pauszek III[b,2], Martin Gustavsson[a,3], Tracy M. Handel[a]*, and David P. Millar[b]*

[a] Skaggs School of Pharmacy and Pharmaceutical Sciences, Department of Pharmacology, University of California San Diego, La Jolla, CA 92037.
[b] Department of Integrative Structural and Computational Biology, The Scripps Research Institute, La Jolla, CA 92037.
[1] Present address: Amsterdam Institute for Molecular and Life Sciences, Department of Medicinal Chemistry, Faculty of Science, Vrije Universiteit Amsterdam, 1081 HV Amsterdam, Netherlands
[2] Present address: LUMICKS, 1105 AG Amsterdam, Netherlands
[3] Present address: Department of Biomedical Sciences, Faculty of Health and Medical Sciences, University of Copenhagen, 2200 Copenhagen, Denmark

*Correspondence and requests for materials should be addressed to D.P.M. (millar@scripps.edu) or T.M.H. (thandel@health.ucsd.edu)

Keywords: Chemokine receptor, single-molecule FRET, GPCR, ACKR3, conformational dynamics

This PDF file includes:

Main Text
Figures 1 to 6

Abstract

The canonical chemokine receptor CXCR4 and atypical receptor ACKR3 both respond to CXCL12 but induce different effector responses to regulate cell migration. While CXCR4 couples to G proteins and directly promotes cell migration, ACKR3 is G protein-independent and scavenges CXCL12 to regulate extracellular chemokine levels and maintain CXCR4 responsiveness, thereby indirectly influencing migration. The receptors also have distinct activation requirements. CXCR4 only responds to wild-type CXCL12 and is sensitive to mutation of the chemokine. By contrast, ACKR3 recruits GPCR kinases (GRKs) and β-arrestins and promiscuously responds to CXCL12, CXCL12 variants, other peptides and proteins, and is relatively insensitive to mutation. To investigate the role of conformational dynamics in the distinct pharmacological behaviors of CXCR4 and ACKR3, we employed single-molecule FRET to track discrete conformational states of the receptors in real-time. The data revealed that apo-CXCR4 preferentially populates a high-FRET inactive state, while apo-ACKR3 shows little conformational preference and high transition probabilities among multiple inactive, intermediate and active conformations, consistent with its propensity for activation. Multiple active-like ACKR3 conformations are populated in response to agonists, compared to the single CXCR4 active-state. This and the markedly different conformational landscapes of the receptors suggest that activation of ACKR3 may be achieved by a broader distribution of conformational states than CXCR4. Much of the conformational heterogeneity of ACKR3 is linked to a single residue that differs between ACKR3 and CXCR4. The dynamic properties of ACKR3 may underly its inability to form productive interactions with G proteins that would drive canonical GPCR signaling.

Main Text

Introduction

CXC chemokine receptor 4 (CXCR4) is one of the most intensively studied chemokine receptors due to its central role in driving cell migration during development and immune responses, and in cancer where it promotes tumor growth and metastasis (1-4). As a class A G protein-coupled receptor (GPCR), CXCR4 activates inhibitory Gαi protein signaling pathways to directly control cell movement in response to the chemokine CXCL12 (5). The activated receptor is also phosphorylated by GPCR kinases (GRKs), which promotes arrestin recruitment and cessation of the G protein signal. CXCR4 often works together with atypical chemokine receptor 3 (ACKR3, formerly CXCR7) which indirectly influences migration by scavenging CXCL12 to regulate available extracellular levels of the agonist and in turn the responsiveness of CXCR4 (6-8). In the absence of ACKR3 scavenging, excessive CXCL12 stimulation of CXCR4 leads to downregulation, resulting in profound effects on neuronal cell migration and development (9-11).

In contrast to CXCR4 and with some exceptions noted (12, 13), ACKR3 lacks G protein activity and instead is considered to be arrestin-biased (14). However, we and others (9) have shown that arrestins are dispensable for chemokine scavenging while GRK phosphorylation is critical for this function (15), suggesting that ACKR3 might be better described as GRK-biased. The molecular basis for its inability to couple to G proteins in most cell types remains an unanswered question. Our recently determined structures of ACKR3-ligand complexes showed the expected hallmarks of GPCR activation including "microswitch residues" in active state configurations, displacement of transmembrane helix 6 (TM6) away from the helical bundle and an open intracellular pocket, consistent with a receptor that should be able to activate G proteins (16). Accordingly, we replaced the intracellular loops (ICLs) of ACKR3 with those of CXCR2, a canonical G protein-coupled chemokine receptor; however, these changes did not lead to G protein activation (16), suggesting that the lack of coupling is not due to the absence of specific residue interactions. CXCL12 also adopts a distinct pose when bound to ACKR3 compared to CXCR4 and all other chemokines in chemokine-receptor complexes, but since small molecules induce similar biased effector responses, the chemokine pose cannot explain the effector-coupling bias (16). Having excluded other mechanisms we therefore surmised that the inability of ACKR3 to activate G proteins may be due to differences in receptor dynamics. Consistent with this hypothesis, the ICLs observed in ACKR3-agonist complexes are disordered, which may preclude productive effector coupling. The dynamic nature of ACKR3 is also suggested by its considerable constitutive activity in recruiting β-arrestins and its high level of constitutive internalization (16-18).

In addition to their distinct effector interactions, ACKR3 and CXCR4 have dramatically different susceptibilities to activation by different ligands. CXCR4 is activated by a single chemokine agonist, CXCL12. Moreover, modifications of the CXCL12 N-terminal signaling domain (e.g. single point mutations as in $CXCL12_{P2G}$ or multiple mutations as in $CXCL12_{LRHQ}$) transform the chemokine into an antagonist (19, 20). Mutational analysis, modeling, and new structures of CXCR4 suggest that ligand activation involves a precise network of interacting residues that stabilize the active receptor conformation (21-25). By contrast, ACKR3 is activated by CXCL12 as well as its variants (including $CXCL12_{P2G}$ and $CXCL12_{LRHQ}$ (19, 20)), other chemokines (CXCL11) (26), other proteins (adrenomedullin, BAM22) (27, 28), and opioid peptides (29). In fact, most ligands for ACKR3 act as agonists, which is best explained by a non-specific "distortion" mechanism of activation

101 whereby any ligand that breaches the binding pocket causes helical movements that are
102 permissive to GRK phosphorylation and arrestin recruitment. A distortion mechanism is
103 consistent with the different binding poses observed for a small molecule agonist
104 compared to the CXCL12 N-terminus in the receptor orthosteric pocket (16), and ligand
105 bulk rather than specific interactions between agonist and ACKR3 being required for
106 activation. We hypothesize that this distortion mechanism would also be facilitated by a
107 receptor that is conformationally dynamic by enabling nonspecific ligand interactions and
108 more than a single conformation to promote activation.
109
110 To investigate the role of conformational dynamics in the distinct pharmacological
111 behaviors of ACKR3 and CXCR4, we developed a single-molecule Förster resonance
112 energy transfer (smFRET) approach. Many ensemble methods such as EPR, NMR and
113 fluorescence-based methods have provided considerable insights into GPCR dynamics,
114 conformational heterogeneity, and exchange between distinct structural states (30-36).
115 However, these methods are limited in their ability to resolve the sequence of state-to-
116 state transitions except in rare cases where transitions can be temporally coordinated with
117 high precision (37). By contrast smFRET enables detection of sparsely populated states,
118 reveals the sequence of state-to-state transitions and provides kinetic information through
119 analysis of state dwell times. For example, smFRET studies of the β_2 adrenergic receptor
120 (β_2AR) revealed a dynamic equilibrium between inactive and active conformations that
121 was responsive to agonist and G protein binding (38). More recent smFRET studies of the
122 glucagon receptor (39), the A_{2A} receptor (A_{2A}R) (40, 41), and the μ-opioid receptor (42)
123 have documented the existence of stable intermediate conformations in addition to
124 inactive and active receptor conformations.
125
126 Here we present the first smFRET study of the chemokine receptors CXCR4 and ACKR3.
127 Our experimental system allows real-time observation of the conformational fluctuations
128 of individual receptor molecules in a native-like lipid environment and assessment of the
129 differences in the conformational dynamics of the two receptors in their apo states and in
130 response to ligands. Our results indicate that ACKR3 is more dynamic and
131 conformationally heterogeneous than CXCR4 or other class A GPCRs previously studied,
132 which may explain its activation prone nature and lack of G protein coupling. In contrast,
133 CXCR4 appears less flexible, consistent with a more restricted, structurally-defined
134 activation mechanism. Together these data characterize the molecular differences
135 between CXCR4 and ACKR3 and suggest that enhanced conformational dynamics plays
136 an important role in the atypical function of ACKR3.
137
138 **Results**
139 Development of smFRET experimental systems for CXCR4 and ACKR3.
140 To visualize conformational fluctuations of CXCR4 and ACKR3 by smFRET, cysteine
141 residues were introduced into CXCR4 at positions $150^{4.40}$ in TM4 and $233^{6.29}$ in TM6, and
142 at $159^{4.40}$ and $245^{6.28}$ in ACKR3 (Figs. S1A & B) (numbers in superscript refer to the
143 Ballesteros-Weinstein numbering scheme for GPCRs) for covalent labeling with FRET
144 donor (D, Alexa Fluor 555, A555) and acceptor (A, Cyanine5, Cy5) fluorophores. Single
145 receptor molecules of labeled CXCR4 or ACKR3 were reconstituted into phospholipid
146 nanodiscs to mimic the native membrane bilayer environment. Nanodiscs have been used
147 in a wide variety of structural and biophysical studies of integral membrane proteins,
148 including ACKR3, and reconstitute protein-lipid interactions lost in detergent systems (43-
149 45). The nanodisc-receptor complexes were then tethered to a quartz slide through

150 biotinylation of the nanodisc membrane scaffolding protein (MSP) (Fig. 1A). To promote
151 monomeric receptor incorporation in each nanodisc, we utilized MSP1E3D1, which forms
152 nanodiscs with a diameter of approximately 13 nm (46, 47).
153
154 Crystal and cryo-electron microscopy (cryo-EM) structures of homologous class A
155 GPCRs, such as β_2AR, in inactive and active conformations, reveal that TM6 moves
156 outwards from the TM helical bundle during activation, whereas the position of TM4
157 remains relatively fixed (48). Accordingly, we anticipated that labeling at the positions
158 indicated above would be sensitive to transitions between inactive and active receptor
159 conformations and give rise to different donor-acceptor distances and FRET efficiencies
160 that could be resolved by smFRET measurements (shown schematically in Fig. 1B).
161 These positions are similar to those used effectively for β_2AR (38), A_{2A}R, (40), and the μ-
162 opioid receptor (42) for monitoring their conformational dynamics by smFRET. Importantly,
163 neither wild-type (WT) CXCR4 nor ACKR3 exhibited significant labeling and the double
164 cysteine receptor mutants retained the ability to recruit β-arrestin2 (Figs. S1C & D).
165
166 <u>ACKR3 exhibits greater conformational dynamics than CXCR4.</u>
167 Receptor-nanodisc complexes were imaged on the slide surface using smFRET
168 microscopy by exciting the A555 donor with a green (532 nm) laser and monitoring the
169 resulting emission from both A555 and the Cy5 acceptor over time on separate segments
170 of a CCD camera. Several hundred individual receptor-nanodisc complexes were typically
171 observed in the field of view. Individual receptor molecules labeled with a single A555
172 donor and a single Cy5 acceptor were identified by single-step photobleaching transitions
173 (abrupt loss of acceptor fluorescence signal or simultaneous loss of fluorescence signal
174 in both channels), as shown for two representative ACKR3-nanodisc complexes in Fig.
175 1C. Additionally, anti-correlated changes in donor and acceptor emission prior to
176 photobleaching confirmed that FRET occurred between A555 and Cy5. Additional
177 examples of single-molecule traces for ACKR3 and CXCR4 are shown in Fig. S2.
178
179 FRET data from many individual receptor-nanodisc complexes, recorded in the presence
180 or absence of different ligands, were globally analyzed using Hidden Markov Models
181 (HMMs) assuming the presence of two, three, four, or five FRET states (Materials and
182 Methods). To evaluate the appropriate level of model complexity, each resulting FRET
183 efficiency distribution was fit with a Gaussian Mixture Model (GMM) and the corresponding
184 Bayesian Information Criterion (BIC) was calculated. The BIC is a statistical measure of
185 the likelihood that the model describes the data while also penalizing the addition of
186 parameters that could lead to overfitting of noise. Theoretically, this value will be at a
187 minimum for the model with the appropriate number of states. As an additional criterion,
188 we carefully compared the FRET distributions recovered for the different models, looking
189 for consistent peak positions across different experimental conditions.
190
191 These analyses indicated that three FRET states were sufficient to fit the smFRET data
192 for CXCR4 under all conditions (Figs. S3 & S4). The resulting FRET efficiency distributions
193 are presented in Figs. 2A & B. The predominant high-FRET state (E = 0.85) observed in
194 the apo-state (Fig. 2A) suggests that TM4 and 6 are in close physical proximity, which is
195 consistent with the conformation of inactive GPCRs (49, 50). Accordingly, we interpret this
196 FRET state as the inactive conformation of CXCR4 and designate it as R. The minor low-
197 FRET state (E = 0.19) reflects outward movement of TM6 away from TM4, as expected
198 for an active receptor conformation (designated R*) (48, 51) and consistent with limited

basal activity of CXCR4. Moreover, there was a major population shift from the high-FRET state to the low-FRET state upon addition of $CXCL12_{WT}$ (Fig. 2B), consistent with the expected stabilization of active GPCR conformations by agonists (52, 53). To gain insight into the nature of the mid-FRET state (E = 0.59), we examined the connectivity between all three FRET states. Two-dimensional transition density probability (TDP) plots revealed that the three FRET states were connected in a sequential fashion (Figs. 2A & B). Notably, non-sequential transitions that "skip over" an intervening FRET state were rarely observed. These results suggest that the mid-FRET state represents an intermediate receptor conformation (designated R') that lies on the pathway between inactive and active conformations. In the apo-state, transitions were mostly observed between states R and R' (Fig. 2A), while in the presence of $CXCL12_{WT}$ the most frequent transitions were observed between the R' and R* states (Fig. 2B).

In contrast, the FRET efficiency histogram for ACKR3 in the apo state (Fig. 2C) was much broader than the corresponding histogram for CXCR4 (Fig. 2A), indicating greater conformational heterogeneity. Moreover, the smFRET data for ACKR3 could not be described by three FRET states and the inclusion of a fourth state was necessary (Figs. S5 & S6). The FRET distributions recovered by four-state global analysis are presented in Figs. 2C & D. The positions of the high-FRET (E = 0.85) and low-FRET (E = 0.11) peaks are similar to those observed in CXCR4 and are likewise assigned to inactive (R) and active (R*) conformations, respectively. Consistent with these assignments, the R* state increased in population at the expense of the R state in the presence of the chemokine agonists $CXCL12_{WT}$ (Fig. 2D) or CXCL11 (Fig. S7B). TDP plots indicated that the four FRET states in ACKR3 were connected in a sequential fashion (Figs. 2C & D). Accordingly, the mid-FRET peaks (E = 0.39 and E = 0.66) are assigned to two intermediate receptor conformations, designated R*' and R', respectively. Notably, the R*' state was not observed in CXCR4 (Figs. 2A & B). The R' state in ACKR3 decreased in population in the presence of chemokine agonists (Fig. 2D, Fig. S7B), suggesting that this state represents an inactive intermediate receptor conformation, consistent with its position on the conformational pathway (closest to R). In striking contrast to apo-CXCR4, apo-ACKR3 populated the four conformational states more or less equally and all possible sequential conformational transitions were observed (Fig. 2C). Thus, ACKR3 is intrinsically more conformationally heterogenous and dynamic than CXCR4. In the presence of $CXCL12_{WT}$, ACKR3 showed more frequent R' ↔ R*' and R*' ↔ R* transitions compared with the apo-receptor, accounting for the population shift towards the R* state (Figs. 2C & D).

<u>Effect of small-molecule ligands on conformational states of CXCR4 and ACKR3.</u>
The small-molecule ligand IT1t is reported to act as an inverse agonist of CXCR4 (51-53). However, the conformational distribution of CXCR4 showed little change with inclusion of IT1t (Figs. 3A & B, Fig. S8), suggesting that it acts as a neutral antagonist in our purified in vitro system. However, R ↔ R' transitions were more probable in the presence of IT1t compared with the apo-receptor (Figs. 3A & B).

Treatment of ACKR3 with the small-molecule agonist VUF15485 (53) shifted the conformational distribution of the receptor towards the active R* state (Figs. S7C & S8), as expected for an agonist and supporting the assignment of the R* FRET state. In contrast, treatment of ACKR3 with the small-molecule inverse agonist VUF16840 (53) shifted the conformational distribution to the inactive R conformation, with a concomitant decrease of R* (Fig. 3D, Fig. S8), consistent with the suppression of the basal activity of

ACKR3 (53). The R*' population also decreased in the presence of the inverse agonist (Fig. 3D, Fig. S8), suggesting that this state represents an active-like receptor conformation, consistent with its placement on the conformational pathway (closest to R*). The suppression of active receptor conformations was also evident in the TDP, which revealed fewer transitions between R*' and R* conformations relative to the apo receptor (Figs. 3C & D).

<u>CXCL12 N-terminal mutants promote active receptor conformations despite their contrasting pharmacological effects on CXCR4 and ACKR3.</u>

CXCR4 is sensitive to N-terminal mutations of CXCL12 while ACKR3 is relatively insensitive. For example, the variant $CXCL12_{P2G}$, containing a proline to glycine mutation in the second position, and $CXCL12_{LRHQ}$, where the first three residues of $CXCL12_{WT}$ are replaced with the four-residue motif LRHQ starting with L0, are antagonists of CXCR4 but agonists of ACKR3 (19, 20). To gain further insight into the ligand-dependent responses of CXCR4 and ACKR3, we examined how these mutant chemokines influence the conformational states and dynamics of both receptors.

Surprisingly, despite acting as a CXCR4 antagonist (20), $CXCL12_{P2G}$ promoted a shift to the active R* conformation of CXCR4 compared to the apo-receptor (R* increased by 16%, Figs. 4A & B, Fig. S8), although the shift was less pronounced than observed for $CXCL12_{WT}$ (28% increase in R*, Fig. 2B, Fig. S8). The shift is also evident in the TDPs where the state-to-state transitions involving the R* active state were more probable for the $CXCL12_{P2G}$ complex compared with apo-CXCR4 (Figs. 4A & B). The presence of $CXCL12_{LRHQ}$ had a more subtle effect on CXCR4: the active R* conformation increased by 9% (Figs. 4A & C, Fig. S8). Despite the ability of $CXCL12_{P2G}$ and $CXCL12_{LRHQ}$ to stabilize the active R* conformation of CXCR4, both variants are known to act as antagonists (20). The implication is that outward movement of TM6 and consequent opening of the intracellular cleft is not sufficient to drive G protein activation of CXCR4. According to a previously proposed model, a precise network of interacting residues within both CXCL12 and CXCR4 is required for receptor activation and signaling (22). Our results reveal that disrupting this network with CXCL12 mutations P2G and LRHQ still promoted the active receptor conformation, suggesting that conformational changes leading to activation can be separated from formation of the interaction network.

In the case of ACKR3, $CXCL12_{P2G}$ induced a modest increase in the population of the active R* conformation relative to the apo-receptor (R* increased by 5%, Figs. 4D & E, Fig. S8), consistent with the ability of this CXCL12 variant to act as an agonist of ACKR3 (20). Additionally, $CXCL12_{P2G}$ also promoted formation of the active-like intermediate R*' conformation (R*' increased by 6%, Figs. 4D & E, Fig. S8), suggesting that activation of ACKR3 can be achieved by populating the R*' state, not just the R* state, which is consistent with a flexible, distortion activation mechanism. Together, $CXCL12_{P2G}$ increased active (R*) and active-like (R*') conformations by 11 %, somewhat less than observed for $CXCL12_{WT}$ (24%, Fig. 2C, Fig. S8). $CXCL12_{LRHQ}$ also promoted the active (R*) and active-like (R*') conformations of ACKR3 (R* + R*' increased by 11%, Fig. 4F, Fig. S8). Additionally, transitions to the active R* and active-like R*' conformations appeared to be more probable in the presence of $CXCL12_{LRHQ}$ compared to $CXCL12_{P2G}$ (Figs. 4E & F), which could be a consequence of its longer residence time on the receptor (54). The agonism observed for both chemokine variants (19, 20) suggests that both the

active R* and active-like R*' conformations of ACKR3 are sufficient for GRK phosphorylation and arrestin recruitment.

ACKR3 constitutive activity is linked to receptor conformational heterogeneity.

As noted above, apo-ACKR3 displays little conformational selectivity, with similar occupancies observed for all four FRET states (Fig. 2C). We hypothesized that this might be related to the constitutive activity of the receptor (13, 16) and tied to the presence of Tyr at position $257^{6.40}$ (Fig. 5A), which is a hydrophobic residue (V, I, or L) in all other chemokine receptors. In many other class A GPCRs, mutating the residue at 6.40 results in constitutive activity (32, 55-57) and previous analysis of rhodopsin suggests that this is a consequence of lowering the energy barrier for transitions between different receptor conformations (58). In our previous work, we showed that mutation of $Y257^{6.40}$ to leucine, the corresponding amino acid in CXCR4, reduces constitutive arrestin recruitment to ACKR3, while preserving the ability of the receptor to be activated by CXCL12 (Fig. S9) (16). Adding this single-point mutation to our ACKR3 smFRET construct had a significant impact, converting the broad conformational distribution of the WT apo-receptor to a narrower distribution concentrated in the high-FRET region (Figs. 5B & C). Overall, the FRET histogram is similar to what we observe for apo-CXCR4 (Fig. 2A), although the active conformation is still split between R* and R*' states (the latter unique to ACKR3) (Fig. 5C). State-to-state transitions were also suppressed relative to WT ACKR3 (Figs. 5B & C). This result indicates that $Y257^{6.40}$ is a major determinant of the broad conformational heterogeneity of ACKR3.

$CXCL12_{WT}$ promoted active-like conformations of $Y257^{6.40}L$ ACKR3 (R* + R*' increased by 16%, Figs. 5C & E), although the effect was somewhat reduced in comparison to WT ACKR3 (R* + R*' increased by 24%, Figs. 5B & D). Consistent with this, the mutant receptor recruits β-arrestin in response to $CXCL12_{WT}$ with an E_{max} value that is only slightly reduced relative to the WT receptor (Fig. S9) (16), suggesting again that the population of the R*' intermediate conformational state may contribute to receptor activation.

Discussion

The molecular basis for the atypical pharmacological behavior of ACKR3 is not well understood. Since structures of ACKR3 show intracellular loop disorder, and progressive structural substitutions within the loops fail to promote G protein coupling (16), we recently proposed that the atypical nature of ACKR3 may be related to receptor conformational dynamics (16, 59). Consistent with this hypothesis, in the present study we found that the conformational dynamics of ACKR3 and the canonical GPCR CXCR4 are indeed markedly different. Our smFRET results revealed four distinct conformations of apo-ACKR3 with approximately equal populations: inactive R, active R*, R' (inactive-like) and R*' (active-like). The state-to-state transition density probability plots (Fig. 2) further reinforced the notion that ACKR3 is a flexible receptor that readily exchanges between different conformational states, consistent with our previous structural studies where a flexible intracellular interface in the absence of interaction partners was observed (16). These observations imply that ACKR3 must have a relatively flat energy landscape, with similar local minima and low energy barriers between states (Fig. 6). The flat energy landscape is consistent with a dynamic receptor that is constitutively active and readily activated. By contrast, our smFRET results reveal that apo-CXCR4 is more conformationally static than ACKR3 and primarily populates an inactive high-FRET conformation with limited transitions and only a single intermediate. Consequently,

CXCR4 must have a more rugged energy landscape with deeper valleys and higher barriers between states (Fig. 6).

The active-like R*' conformational state appears to be unique to ACKR3. This state responds to agonist and inverse agonist ligands in the same manner as the active R* state. In contrast, the single intermediate state in CXCR4 (R') is not responsive to ligands. The presence of both active and active-like conformations in ACKR3 may be responsible for its activation prone nature and ligand promiscuity.

Structural features that make ACKR3 conformationally flexible include Y257$^{6.40}$, which we previously showed contributes to the constitutive activity of ACKR3 (16). Similar to the constitutively active M257$^{6.40}$Y mutant of rhodopsin, Y$^{6.40}$ in ACKR3 stacks against Y$^{5.58}$ and Y$^{7.53}$ and stabilizes the active-like conformation (60). Additionally, the broad conformational distribution and high probability of state-to-state transitions of ACKR3 parallel the dramatically lower energy barrier of the M257$^{6.40}$Y rhodopsin mutant relative to WT rhodopsin (58). By contrast, mutation of Y257$^{6.40}$ to leucine, the corresponding amino acid in CXCR4, promoted the dominance of an inactive high-FRET receptor conformation similar to CXCR4 (Figs. 2A & 5C); it also reduced the transition probabilities (Figs. 5B & C) and the ability of ACKR3 to constitutively recruit arrestin (16).

In addition to the contribution of Y257$^{6.40}$ to the dynamic behavior of ACKR3, a disulfide bond between C34 in the receptor N-terminus and C287 in extracellular loop 3 (ECL3), observed in all other reported chemokine receptor-chemokine structures (61-63) is conspicuously missing in cryo-EM structures of ACKR3 with chemokine and small molecule agonists (16). Furthermore, ACKR3 remains functional in the absence of these cysteines (64) unlike other chemokine receptors (65, 66). The disulfide may constrain the relative positions of TM1 and TM6/7 and the opening of the orthosteric pocket; therefore, its absence may confer ACKR3 with greater conformational flexibility than other chemokine receptors, consistent with our observations. It may also allow ACKR3 to be activated by diverse ligands.

The propensity of ACKR3 to be activated by a diverse range of ligands contrasts with the strict ligand requirements of CXCR4. In principle, ligands could promote activation by providing more energetically favorable binding interactions with the receptor in the active R* or R*' conformations relative to the inactive R or R' conformations. Alternatively, ligands could destabilize the inactive R or R' conformations of the receptor, which would also shift the receptor population to the active conformation(s). Our results do not distinguish between these two possibilities. Regardless, the similar free energies of different receptor conformations in ACKR3 and low energy barriers between them (Fig. 6) implies that relatively little energy is required to switch the receptor from one state to another. Moreover, activation can be achieved by populating either the R* or R*' state. Thus, independent of specific binding poses and receptor interactions, a variety of different ligands may be able to easily tip the balance between different receptor conformations. Such a mechanism would thereby promote activation and explain the observed ligand promiscuity of ACKR3. In contrast, the more rugged energy landscape of CXCR4, with larger free energy differences between R, R', and R* conformations and higher energy barriers between them, would require more ligand binding energy to promote receptor activation to the R* state. Additionally, not only is populating the R* conformation required for activation, it is not sufficient as illustrated for CXCL12$_{P2G}$ in Fig. 4B; instead specific

interactions between the ligand and receptor are required, as borne out by mutagenesis studies (Fig. S10) (21, 23).

Another unusual aspect of ACKR3 behavior is the failure to activate G proteins. Why ACKR3 does not couple to G proteins, at least in most cells, is unclear and not readily explained by differences in primary sequence, since insertion of a DRY box motif and substitution of all ICLs from a canonical GPCR failed to confer G protein activity (16). It is possible that the active receptor conformation clashes sterically with the G protein as suggested by docking of G proteins to structures of ACKR3 (16). Alternatively, the receptor dynamics and conformational transitions revealed here may prevent formation of productive contacts between ACKR3 and G protein that are required for coupling, even though G proteins appear to constitutively associate with the receptor (13, 16, 67). Lack of a well-organized intracellular pocket due to frequent conformational transitions may also explain why the fingerloop of arrestin is not observed to interact with the pocket, in contrast with other GPCRs (68, 69), but instead inserts into membranes/micelles adjacent to the receptor (59). Nevertheless, arrestins are still recruited to CXCL12-stimulated ACKR3 due to GRK phosphorylation of the receptor C-terminal tail (15, 70). Since GRKs also interact with the cytoplasmic pocket to facilitate phosphorylation, it remains to be determined how dynamics might decouple G protein activation and arrestin binding to the receptor cytoplasmic pocket (59) while supporting pocket-mediated GRK activity. However, given the fleeting interaction between GRKs and GPCRs (71), rapid state sampling by ACKR3 may not necessarily be detrimental to GRK engagement and phosphorylation. Furthermore, conformational intermediates in addition to the fully active receptor have been shown to be targets for GRK phosphorylation, such as the early photoactivated rhodopsin metarhodopsin I (72). A more constrained system may be necessary to promote productive interactions between ACKR3 and G proteins. Along these lines, a local increase of membrane pressure in certain cell environments could explain the apparent ability of ACKR3 to activate G proteins in astrocytes and glioma cells (12, 13).

The pharmacological behavior of ACKR3 resembles the human cytomegalovirus chemokine receptor US28, which also recognizes diverse chemokines, constitutively internalizes, and displays multiple functional conformations (73). Similar to ACKR3, US28 appears to be activated by distortion of the orthosteric binding pocket rather than by specific side chain contacts between receptor and ligand, which is supported by multiple active conformations observed for both apo-US28 and US28 with different agonists (73-76). Whether US28 also has a relatively flat energy landscape like ACKR3 remains to be seen. Such conformational dynamics and activation mechanisms may also be operative in other chemokine receptors that respond to multiple ligands and have considerable constitutive activity such as CCR1, CCR2 and CCR3 (61, 77). Finally, the ability of ACKR3 to be easily activated by populating more than one conformational state may explain why antagonizing the receptor by targeting the orthosteric binding pocket has proven to be challenging; in contrast the specific requirements for CXCR4 agonism has permitted the development of many orthosteric antagonists but few agonists (78). Drug discovery efforts aimed at inhibiting ACKR3 may therefore require allosteric strategies.

Materials and Methods

Unless otherwise stated all chemicals and reagents were purchased from SigmaAldrich or Fisher Scientific. Methoxy e-Coelenterazine (Prolume Purple) was purchased from Nanolight Technologies (Prolume LTD).

443
444 Cloning
445 ACKR3 (residues 2-362) preceded by an N-terminal HA signal sequence and followed by
446 C-terminal 10His and FLAG tags was cloned into the pFasBac vector for purification from
447 *Sf9* cells. CXCR4 (residues 2-352) with an N-terminal FLAG tag and C-terminal 10His was
448 inserted into pFasBac for purification. For cell-based assays, ACKR3 (residues 2-362) or
449 CXCR4 (residues 2-352) were inserted into pcDNA3.1 expression vector with an N-
450 terminal FLAG tag and followed with a C-terminal *Renilla* luciferase II (ACKR3_rlucII and
451 CXCR4_rlucII). Site-directed mutagenesis was performed by overlap extension and
452 confirmed by Sanger sequencing.
453
454 Arrestin recruitment by BRET
455 Arrestin recruitment to ACKR3 and CXCR4 was detected using a BRET2 assay as
456 previously described (15, 54). Briefly, HEK293T cells (ATCC) were plated at 750k/well in
457 a 6-well dish in Dulbecco's modified eagle media (DMEM) with 10% fetal bovine serum
458 (FBS) and transfected 24 hrs later with 50 ng receptor_rlucII DNA, 1 µg GFP10_β-
459 arrestin2 (a kind gift from N. Heveker, Université de Montréal, Canada), and 1.4 µg empty
460 pcDNA3.1 vector using TransIT-LT1 transfection system (MirusBio) and expressed for 40
461 hrs. The cells were then washed with PBS (137 mM NaCl, 2.7 mM KCl, 10 mM Na_2HPO_4,
462 1.8 mM KH_2PO_4, pH 7.4) and mechanically lifted in Tyrode's buffer (25 mM HEPES, 140
463 mM NaCl, 1 mM $CaCl_2$, 2.7 mM KCl, 12 mM $NaHCO_3$, 5.6 mM Glucose, 0.5 mM $MgCl_2$,
464 0.37 mM NaH_2PO_4, pH 7.5). 100k cells were plated per 96-well white BRET plate (BD
465 Fisher) and reattached for 45 min at 37 °C. GFP expression was checked using a
466 SpectraMax M5 plate fluorometer (Molecular Devices) with 485 nm excitation, 538 nm
467 emission, and 530 nm cutoff. 5 µM Prolume Purple substrate was subsequently added
468 and total luminescence detected using a TECAN Spark Luminometer (TECAN Life
469 Sciences) at 37 °C. CXCL12 was then added to each well at the indicated final
470 concentrations and BRET was read using default BRET2 settings (blue emission 360-440
471 nm, red emission 505-575 nm) and an integration time of 0.5 sec. Experiments were
472 baseline matched and normalized to the E_{max} of WT receptor. The reported data is the
473 average of three independent experiments performed in duplicate. Points were fit to a
474 sigmoidal dose-response model using SigmaPlot 11.0 (Systat Software, Inc).
475
476 Receptor purification, labeling, and nanodisc reconstitution
477 $M159^{4.40}C/Q245^{6.28}C$ ACKR3 (WT and $Y257^{6.40}L$) and $L150^{4.40}C/Q233^{6.29}C$ CXCR4 were
478 purified from *Sf9* cells (Expression Systems) as previously described (16). Briefly, *Sf9* cells
479 were infected with baculovirus (prepared using Bac-to-Bac Baculovirus Expression
480 System, Invitrogen) containing either the mutant ACKR3 or CXCR4. Cells were harvested
481 after 48 hrs and membranes dounce homogenized in hypotonic buffer (10 mM HEPES pH
482 7.5, 10 mM $MgCl_2$, 20 mM KCl) followed three more times with hypotonic buffer with 1 M
483 NaCl. The membranes were spun down at 50k x g for 30 min and resuspended between
484 each round of douncing. After the final round, membranes were incubated with 100 µM
485 CCX662 (Chemocentryx Inc.) for ACKR3 or 100 µM IT1t for CXCR4 and solubilized in 50
486 mM HEPES pH 7.5, 400 mM NaCl, 0.75/0.15% dodecyl maltoside/cholesteryl
487 hemisuccinate (DDM/CHS) with a protease inhibitor tablet (Roche) for 4 hrs. Insoluble
488 material was then removed by centrifugation at 50k x g for 30 min and Talon resin
489 (Clontech) with 20 mM imidazole overnight binding at 4 °C. The resin was then transferred
490 to a column and washed with WB1 (50 mM HEPES pH 7.5, 400 mM NaCl, 0.1/0.02%
491 DDM/CHS, 10% glycerol, 20 mM imidazole) followed by WB2 (WB1 with 0.025/0.005%

492 DDM/CHS) and finally eluted with WB2 with 250 mM imidazole. The imidazole was
493 removed by desalting column (PD MiniTrap G-25, GE Healthcare). Final protein
494 concentration was determined by A_{280} using an extinction coefficient of 75000 $M^{-1}cm^{-1}$
495 (ACKR3) and 58850 $M^{-1}cm^{-1}$ (CXCR4). Samples were snap frozen in liquid nitrogen, and
496 stored at -80 °C until use.
497
498 When ready to prepare samples for smFRET measurements, two nanomoles of receptor
499 was thawed and incubated with fourteen nanomoles of Alexa Fluor 555 (A555) and Cy5
500 overnight at 4 °C with rotation. The next morning, free label was removed by dilution using
501 a 100k Da cut-off spin concentrator (Amicon) and the sample concentrated to ~100 µl.
502 Label incorporation was evaluated by measuring the absorbance at A_{280} (ε_{280} = 75000 M^{-}
503 $^{1}cm^{-1}$ for ACKR3 and 58850 $M^{-1}cm^{-1}$ for CXCR4), A_{555} (ε_{555} = 150000 $M^{-1}cm^{-1}$), and A_{645}
504 (ε_{645} = 250000 $M^{-1}cm^{-1}$) to detect the concentrations of the labeled receptor, A555, and
505 Cy5, respectively. The contribution of the fluorophores to A_{280} was removed before
506 determining labeled receptor concentration. The entire sample was used for nanodisc
507 reconstitution.
508
509 Labeled receptors were reconstituted into biotinylated MSP1E3D1 nanodiscs as
510 previously described (16). Briefly, 1-palmitoyl-2-oleoyl-*sn*-glycero-3-phosphocholine
511 (POPC, Avanti) and 1-palmitoyl-2-oleoyl-*sn*-glycero-3-phospho-(1'-rac-glycerol) (POPG,
512 Avanti) were prepared in a 3:2 POPC:POPG ratio and solubilized in ND buffer (25 mM
513 HEPES pH 7.5, 150 mM NaCl, 180 mM cholate). MSP1E3D1 was expressed and purified
514 as previously described (79) and biotinylated with EZ-Link NHS-polyethylene glycol 4
515 (PEG4)-Biotin (Thermo Fisher) per manufacturer instructions. The receptors, MSP1E3D1,
516 and lipids were combined at a molar ratio of 0.1:1:110 for ACKR3:MSP:lipids respectively.
517 Additional ND buffer was added to keep the final cholate concentration >20 mM. After 30
518 min at 4 °C, 200 mg of Biobeads (Bio-Rad) were added and incubated for 3-6 hrs. The
519 sample was then loaded on a Superdex 200 10/300 GL column equilibrated with 25 mM
520 HEPES pH 7.5, 150 mM NaCl and fractions containing nanodisc complexes were
521 combined. 200 µl Talon resin was added with 20 mM imidazole (final concentration) and
522 the samples were incubated for 16 hrs at 4 °C. The resin was then transferred to a Micro
523 Bio-Spin Column (Bio-Rad) and washed with 25 mM HEPES pH 7.5, 150 mM NaCl, 20
524 mM imidazole and eluted with 25 mM HEPES pH 7.5, 150 mM NaCl, 250 mM imidazole.
525 Imidazole was removed by buffer-exchange using 100k Da spin concentrators and 25 mM
526 HEPES pH 7.5, 150 mM NaCl. Sample were concentrated to ~1 µM and stored at 4 °C
527 until use.
528
529 <u>CXCL12 purification from *E. Coli*</u>
530 CXCL12 was expressed and purified as previously described (15, 16). Briefly, the
531 chemokines were expressed by IPTG induction in BL21(DE3)pLysS cells. The cells were
532 collected by centrifugation, resuspended in 50 mM tris pH 7.5, 150 mM NaCl and lysed by
533 sonication. Inclusion bodies were then collected by centrifugation, resuspended in
534 equilibration buffer (50 mM tris, 6 M guanidine-HCl pH 8.0), sonicated to release the
535 chemokines and the samples centrifuged again to pellet insoluble material. The
536 supernatant was then passed over a Ni-nitrilotriacetic acid (NTA) column equilibrated with
537 equilibration buffer to bind the His-tagged chemokines. The column was washed with
538 wash buffer (50 mM MES pH 6.0, 6 M guanidine-HCl) and eluted with 50 mM acetate pH
539 4.0, 6 M guanidine-HCl. The chemokine-containing elutions were pooled and dithiothreitol
540 (DTT) added to a final concentration of 4 mM. After incubating 10 min, the solution was

541 added dropwise into refolding buffer (50 mM tris pH 7.5, 500 mM arginine-HCl, 1 mM
542 EDTA, 1 mM oxidized glutathione) and incubated at room temperature for 4 hrs before
543 dialyzing against 20 mM tris pH 8.0, 50 mM NaCl. To remove the N-terminal purification
544 tag, enterokinase was added and the sample incubated at 37 °C for 5 days. Uncleaved
545 chemokine and free tags were removed by reverse Ni-NTA and eluted with wash buffer.
546 Finally, the sample was purified on a reverse-phase C18 column equilibrated with 75%
547 buffer A (0.1% trifluoroacetic acid (TFA)) and 25% buffer B (0.1% TFA, 90% acetonitrile)
548 and eluted by a linear gradient of buffer B. The pure protein was lyophilized and stored at
549 -80 °C until use.
550
551 smFRET microscopy
552 smFRET experiments were performed on a custom built prism-based TIRF microscope
553 as previously described (80). Briefly, a flow cell was assembled on a quartz slide
554 passivated with polyethylene glycol (PEG) and a small fraction of biotinylated PEG, after
555 which neutravidin was introduced (81). Labeled ACKR3 or CXCR4 in biotinylated
556 nanodiscs were diluted into trolox buffer (25 mM HEPES pH 7.5, 150 mM NaCl, 1 mM
557 propyl gallate, 5 mM trolox), flowed into the sample chamber, and incubated for 5 min at
558 room temperature. The samples were then washed twice with imaging buffer (trolox buffer
559 with 2 mM protocatechuic acid, 50 nM protocatechuate-3,4-dioxygenase). Movies were
560 collected with 100 ms integration time using a custom single-molecule data acquisition
561 program to control the CCD camera (Andor). Single-molecule donor and acceptor
562 emission traces were extracted from the recordings using custom IDL (Interactive Data
563 Language) scripts. The software packages used to control the CCD camera and extract
564 time trajectories were provided by Dr. Taekjip Ha. In all cases, five initial apo-receptor
565 movies were recorded at different locations on the slide and then ligand was flowed into
566 the cell by two washes with chemokine or small molecule in imaging buffer at final
567 concentrations of 500 nM for chemokines ($CXCL12_{WT}$, $CXCL12_{P2G}$, $CXCL12_{LRHQ}$,
568 CXCL11) and 1 μM for the small molecules (IT1t, VUF16840, VUF15485). Ten more
569 movies were collected for each condition at different locations on the slide. The data
570 presented are a composite of at least three individual slides and treatments.
571
572 FRET trajectories were generated and analyzed using custom software written in-house
573 (https://github.com/rpauszek/smtirf). Donor and acceptor traces for each molecule were
574 corrected for donor bleed through and background signal and FRET efficiencies were
575 calculated as $E = I_A/(I_A+I_D)$, where E is the apparent FRET efficiency at each time point
576 and I_D and I_A are the corresponding donor and acceptor fluorophore intensities,
577 respectively. Traces were screened manually for single donor and acceptor bleach steps
578 and anti-correlated behavior between fluorophores to confirm the presence of single
579 receptors within the identified particles and single donor and acceptor labeling. All traces
580 for a particular protein/ligand combination were analyzed globally by a single Hidden
581 Markov Model assuming two, three, four, or five states and shared variance as previously
582 described (80). Briefly, each model was trained on all selected trajectories for a given
583 sample simultaneously using an expectation-maximization method (82). Once a model
584 was trained, the Viterbi algorithm (82) was used to determine the most likely hidden path
585 for each trajectory. This labeled state path was then used to aggregate all data points
586 belonging to a particular state in order to compile composite histograms of FRET
587 efficiency, using a Kernel Density estimation algorithm (Python package Scikit-learn,
588 version 1.2.2) with a Gaussian kernel and a bandwidth of 0.04. The relative populations
589 of distinct FRET states were directly obtained during compilation of the corresponding

histograms. The resulting FRET efficiency histograms were fit with a Gaussian Mixture Model (Scikit-learn) and the corresponding Bayesian Information Criterion (BIC) was calculated as described (83). Transition density probability plots revealing the connectivity among individual FRET states were calculated as described (84).

Data availability

All relevant data supporting this study are included in the Article or Supplementary files and are available from the authors upon request.

Acknowledgments

We gratefully acknowledge the initial work on this project undertaken by Chunxia Zhao and Rajan Lamichhane. Additionally, we thank Handel lab members Cheyanne Shinn, Catherina Salanga, and Nicholas Chimileski for providing the chemokines CXCL11 and $CXCL12_{P2G}$, respectively, R. Leurs (Vrije Universiteit Amsterdam) for the small molecules VUF16840 and VUF15485, and N. Heveker (Université de Montréal) for the β-arrestin2_GFP10 plasmid. This work was supported by R01 GM133157 (D.P.M./T.M.H), R01 CA254402 (T.M.H.), R01 AI161880 (T.M.H.), F32 GM137505 (C.T.S.), Robertson Foundation/Cancer Research Institute Irvington Postdoctoral Fellowship (M.G.), F32 GM115017 and T32 AI007354 (R.F.P.).

Author Contributions:

Conception and design of the research: C.T.S., T.M.H., and D.P.M.
Methodology: C.T.S., R.F.P., and M.G.
Software: R.F.P.
Validation: C.T.S. and R.F.P.
Formal Analysis: C.T.S. and R.F.P.
Investigation: C.T.S.
Writing-Original Draft Preparation: C.T.S., T.M.H., and D.P.M.
Writing-Reviewing & Editing: C.T.S., R.F.P., M.G., T.M.H., and D.P.M.
Visualization: C.T.S. and R.F.P.
Supervision: T.M.H. and D.P.M.
Funding Acquisition: T.M.H. and D.P.M.

Competing Interest Statement: T.M.H. is a cofounder of Lassogen Inc. and serves on the Scientific Advisory Boards of Abilita Bio, and Abalone Bio. The terms of these arrangements have been reviewed and approved by the University of California, San Diego in accordance with its conflict of interest policies. The other authors declare that they have no competing interests.

References

1. S. Chatterjee, B. Behnam Azad, S. Nimmagadda, The intricate role of CXCR4 in cancer. *Adv Cancer Res* **124**, 31-82 (2014).
2. F. Balkwill, The significance of cancer cell expression of the chemokine receptor CXCR4. *Semin Cancer Biol* **14**, 171-179 (2004).
3. U. M. Domanska *et al.*, A review on CXCR4/CXCL12 axis in oncology: no place to hide. *Eur J Cancer* **49**, 219-230 (2013).
4. N. Kawaguchi, T. T. Zhang, T. Nakanishi, Involvement of CXCR4 in Normal and Abnormal Development. *Cells* **8** (2019).

638 5. I. Kufareva, M. Gustavsson, Y. Zheng, B. S. Stephens, T. M. Handel, What Do
639 Structures Tell Us About Chemokine Receptor Function and Antagonism? *Annu*
640 *Rev Biophys* **46**, 175-198 (2017).
641 6. J. W. Griffith, C. L. Sokol, A. D. Luster, Chemokines and chemokine receptors:
642 positioning cells for host defense and immunity. *Annu Rev Immunol* **32**, 659-702
643 (2014).
644 7. R. J. Nibbs, G. J. Graham, Immune regulation by atypical chemokine receptors.
645 *Nat Rev Immunol* **13**, 815-829 (2013).
646 8. A. Vacchini, M. Locati, E. M. Borroni, Overview and potential unifying themes of
647 the atypical chemokine receptor family. *J Leukoc Biol* **99**, 883-892 (2016).
648 9. F. Saaber *et al.*, ACKR3 Regulation of Neuronal Migration Requires ACKR3
649 Phosphorylation, but Not beta-Arrestin. *Cell Rep* **26**, 1473-1488 e1479 (2019).
650 10. S. Lau *et al.*, A negative-feedback loop maintains optimal chemokine
651 concentrations for directional cell migration. *Nat Cell Biol* **22**, 266-273 (2020).
652 11. M. Wong *et al.*, Dynamic Buffering of Extracellular Chemokine by a Dedicated
653 Scavenger Pathway Enables Robust Adaptation during Directed Tissue
654 Migration. *Dev Cell* **52**, 492-508 e410 (2020).
655 12. V. Odemis *et al.*, The presumed atypical chemokine receptor CXCR7 signals
656 through G(i/o) proteins in primary rodent astrocytes and human glioma cells. *Glia*
657 **60**, 372-381 (2012).
658 13. A. Fumagalli *et al.*, The atypical chemokine receptor 3 interacts with Connexin 43
659 inhibiting astrocytic gap junctional intercellular communication. *Nat Commun* **11**,
660 4855 (2020).
661 14. S. Rajagopal *et al.*, Beta-arrestin- but not G protein-mediated signaling by the
662 "decoy" receptor CXCR7. *Proc Natl Acad Sci U S A* **107**, 628-632 (2010).
663 15. C. T. Schafer, Q. Chen, J. J. G. Tesmer, T. M. Handel, Atypical Chemokine
664 Receptor 3 'Senses' CXC Chemokine Receptor 4 Activation Through GPCR
665 Kinase Phosphorylation. *Mol Pharmacol* 10.1124/molpharm.123.000710 (2023).
666 16. Y. C. Yen *et al.*, Structures of atypical chemokine receptor 3 reveal the basis for
667 its promiscuity and signaling bias. *Sci Adv* **8**, eabn8063 (2022).
668 17. B. E. Hopkins *et al.*, Effects of Small Molecule Ligands on ACKR3 Receptors.
669 *Mol Pharmacol* **102**, 128-138 (2022).
670 18. U. Naumann *et al.*, CXCR7 functions as a scavenger for CXCL12 and CXCL11.
671 *PLoS One* **5**, e9175 (2010).
672 19. M. S. Hanes *et al.*, Dual targeting of the chemokine receptors CXCR4 and
673 ACKR3 with novel engineered chemokines. *J Biol Chem* **290**, 22385-22397
674 (2015).
675 20. A. Jaracz-Ros *et al.*, Differential activity and selectivity of N-terminal modified
676 CXCL12 chemokines at the CXCR4 and ACKR3 receptors. *J Leukoc Biol*
677 10.1002/JLB.2MA0320-383RR (2020).
678 21. T. Ngo *et al.*, Crosslinking-guided geometry of a complete CXC receptor-
679 chemokine complex and the basis of chemokine subfamily selectivity. *PLoS Biol*
680 **18**, e3000656 (2020).
681 22. M. P. Wescott *et al.*, Signal transmission through the CXC chemokine receptor 4
682 (CXCR4) transmembrane helices. *Proc Natl Acad Sci U S A* **113**, 9928-9933
683 (2016).
684 23. B. S. Stephens, T. Ngo, I. Kufareva, T. M. Handel, Functional anatomy of the full-
685 length CXCR4-CXCL12 complex systematically dissected by quantitative model-
686 guided mutagenesis. *Sci Signal* **13** (2020).

687 24. K. Saotome *et al.*, Structural insights into CXCR4 modulation and
688 oligomerization. *bioRxiv* 10.1101/2024.02.09.579708 (2024).
689 25. Y. Liu *et al.*, Cryo-EM structure of monomeric CXCL12-bound CXCR4 in active
690 state. *bioRxiv* (2023).
691 26. J. M. Burns *et al.*, A novel chemokine receptor for SDF-1 and I-TAC involved in
692 cell survival, cell adhesion, and tumor development. *J Exp Med* **203**, 2201-2213
693 (2006).
694 27. K. R. Klein *et al.*, Decoy receptor CXCR7 modulates adrenomedullin-mediated
695 cardiac and lymphatic vascular development. *Dev Cell* **30**, 528-540 (2014).
696 28. Y. Ikeda, H. Kumagai, A. Skach, M. Sato, M. Yanagisawa, Modulation of
697 circadian glucocorticoid oscillation via adrenal opioid-CXCR7 signaling alters
698 emotional behavior. *Cell* **155**, 1323-1336 (2013).
699 29. M. Meyrath *et al.*, The atypical chemokine receptor ACKR3/CXCR7 is a broad-
700 spectrum scavenger for opioid peptides. *Nat Commun* **11**, 3033 (2020).
701 30. J. J. Liu, R. Horst, V. Katritch, R. C. Stevens, K. Wuthrich, Biased signaling
702 pathways in beta2-adrenergic receptor characterized by 19F-NMR. *Science* **335**,
703 1106-1110 (2012).
704 31. L. M. Wingler *et al.*, Angiotensin Analogs with Divergent Bias Stabilize Distinct
705 Receptor Conformations. *Cell* **176**, 468-478 e411 (2019).
706 32. J. F. Fay, D. L. Farrens, Structural dynamics and energetics underlying allosteric
707 inactivation of the cannabinoid receptor CB1. *Proc Natl Acad Sci U S A* **112**,
708 8469-8474 (2015).
709 33. X. Yao *et al.*, Coupling ligand structure to specific conformational switches in the
710 beta2-adrenoceptor. *Nat Chem Biol* **2**, 417-422 (2006).
711 34. M. Elgeti, W. L. Hubbell, DEER Analysis of GPCR Conformational Heterogeneity.
712 *Biomolecules* **11** (2021).
713 35. L. M. Wingler *et al.*, Angiotensin and biased analogs induce structurally distinct
714 active conformations within a GPCR. *Science* **367**, 888-892 (2020).
715 36. A. P. Ray, N. Thakur, N. G. Pour, M. T. Eddy, Dual mechanisms of cholesterol-
716 GPCR interactions that depend on membrane phospholipid composition.
717 *Structure* **31**, 836-847 e836 (2023).
718 37. C. T. Schafer, J. F. Fay, J. M. Janz, D. L. Farrens, Decay of an active GPCR:
719 Conformational dynamics govern agonist rebinding and persistence of an active,
720 yet empty, receptor state. *Proc Natl Acad Sci U S A* **113**, 11961-11966 (2016).
721 38. G. G. Gregorio *et al.*, Single-molecule analysis of ligand efficacy in beta(2)AR-G-
722 protein activation. *Nature* **547**, 68-73 (2017).
723 39. K. Krishna Kumar *et al.*, Negative allosteric modulation of the glucagon receptor
724 by RAMP2. *Cell* **186**, 1465-1477 e1418 (2023).
725 40. D. D. Fernandes *et al.*, Ligand modulation of the conformational dynamics of the
726 A(2A) adenosine receptor revealed by single-molecule fluorescence. *Sci Rep* **11**,
727 5910 (2021).
728 41. I. Maslov *et al.*, Sub-millisecond conformational dynamics of the A(2A) adenosine
729 receptor revealed by single-molecule FRET. *Commun Biol* **6**, 362 (2023).
730 42. J. Zhao *et al.*, Ligand efficacy modulates conformational dynamics of the micro-
731 opioid receptor. *Nature* 10.1038/s41586-024-07295-2 (2024).
732 43. I. G. Denisov, S. G. Sligar, Nanodiscs for structural and functional studies of
733 membrane proteins. *Nat Struct Mol Biol* **23**, 481-486 (2016).
734 44. I. G. Denisov, S. G. Sligar, Nanodiscs in Membrane Biochemistry and
735 Biophysics. *Chem Rev* **117**, 4669-4713 (2017).

736 45. S. A. Eberle, M. Gustavsson, Bilayer lipids modulate ligand binding to atypical
737 chemokine receptor 3. *Structure* 10.1016/j.str.2024.04.018 (2024).
738 46. H. Tsukamoto, A. Sinha, M. DeWitt, D. L. Farrens, Monomeric rhodopsin is the
739 minimal functional unit required for arrestin binding. *J Mol Biol* **399**, 501-511
740 (2010).
741 47. S. A. Eberle, M. Gustavsson, A Scintillation Proximity Assay for Real-Time
742 Kinetic Analysis of Chemokine-Chemokine Receptor Interactions. *Cells* **11**
743 (2022).
744 48. S. G. Rasmussen *et al.*, Crystal structure of the beta2 adrenergic receptor-Gs
745 protein complex. *Nature* **477**, 549-555 (2011).
746 49. K. Palczewski *et al.*, Crystal structure of rhodopsin: A G protein-coupled receptor.
747 *Science* **289**, 739-745 (2000).
748 50. S. G. Rasmussen *et al.*, Crystal structure of the human beta2 adrenergic G-
749 protein-coupled receptor. *Nature* **450**, 383-387 (2007).
750 51. D. L. Farrens, C. Altenbach, K. Yang, W. L. Hubbell, H. G. Khorana,
751 Requirement of rigid-body motion of transmembrane helices for light activation of
752 rhodopsin. *Science* **274**, 768-770 (1996).
753 52. A. B. Kleist *et al.*, Conformational selection guides beta-arrestin recruitment at a
754 biased G protein-coupled receptor. *Science* **377**, 222-228 (2022).
755 53. O. Otun *et al.*, Conformational dynamics underlying Atypical Chemokine
756 Receptor 3 activation. *BioRxiv* (2023).
757 54. M. Gustavsson, D. P. Dyer, C. Zhao, T. M. Handel, Kinetics of CXCL12 binding
758 to atypical chemokine receptor 3 reveal a role for the receptor N terminus in
759 chemokine binding. *Sci Signal* **12** (2019).
760 55. M. Han, S. O. Smith, T. P. Sakmar, Constitutive activation of opsin by mutation of
761 methionine 257 on transmembrane helix 6. *Biochemistry* **37**, 8253-8261 (1998).
762 56. X. Han, S. D. Tachado, H. Koziel, W. A. Boisvert, Leu128(3.43) (I128) and
763 Val247(6.40) (V247) of CXCR1 are critical amino acid residues for g protein
764 coupling and receptor activation. *PLoS One* **7**, e42765 (2012).
765 57. M. Cui *et al.*, Crystal structure of a constitutive active mutant of adenosine A(2A)
766 receptor. *IUCrJ* **9**, 333-341 (2022).
767 58. H. Tsukamoto, D. L. Farrens, A constitutively activating mutation alters the
768 dynamics of a key conformational change in a ligand-free GPCR. *J Biol Chem*
769 10.1074/jbc.M113.472464 (2013).
770 59. Q. Chen *et al.*, ACKR3-arrestin2/3 complexes reveal molecular consequences of
771 GRK-dependent barcoding. *bioRxiv* 10.1101/2023.07.18.549504 (2023).
772 60. X. Deupi *et al.*, Stabilized G protein binding site in the structure of constitutively
773 active metarhodopsin-II. *Proc Natl Acad Sci U S A* **109**, 119-124 (2012).
774 61. Z. Shao *et al.*, Molecular insights into ligand recognition and activation of
775 chemokine receptors CCR2 and CCR3. *Cell Discov* **8**, 44 (2022).
776 62. L. Qin *et al.*, Structural biology. Crystal structure of the chemokine receptor
777 CXCR4 in complex with a viral chemokine. *Science* **347**, 1117-1122 (2015).
778 63. K. Liu *et al.*, Structural basis of CXC chemokine receptor 2 activation and
779 signalling. *Nature* **585**, 135-140 (2020).
780 64. M. Szpakowska *et al.*, Mutational analysis of the extracellular disulphide bridges
781 of the atypical chemokine receptor ACKR3/CXCR7 uncovers multiple binding
782 and activation modes for its chemokine and endogenous non-chemokine
783 agonists. *Biochem Pharmacol* **153**, 299-309 (2018).

784 65. L. S. Ai, F. Liao, Mutating the four extracellular cysteines in the chemokine
785 receptor CCR6 reveals their differing roles in receptor trafficking, ligand binding,
786 and signaling. *Biochemistry* **41**, 8332-8341 (2002).
787 66. C. Limatola *et al.*, Cysteine residues are critical for chemokine receptor CXCR2
788 functional properties. *Exp Cell Res* **307**, 65-75 (2005).
789 67. A. Levoye, K. Balabanian, F. Baleux, F. Bachelerie, B. Lagane, CXCR7
790 heterodimerizes with CXCR4 and regulates CXCL12-mediated G protein
791 signaling. *Blood* **113**, 6085-6093 (2009).
792 68. D. P. Staus *et al.*, Structure of the M2 muscarinic receptor-beta-arrestin complex
793 in a lipid nanodisc. *Nature* **579**, 297-302 (2020).
794 69. W. Huang *et al.*, Structure of the neurotensin receptor 1 in complex with beta-
795 arrestin 1. *Nature* **579**, 303-308 (2020).
796 70. P. Sarma *et al.*, Molecular insights into intrinsic transducer-coupling bias in the
797 CXCR4-CXCR7 system. *Nat Commun* **14**, 4808 (2023).
798 71. A. Pulvermuller, K. Palczewski, K. P. Hofmann, Interaction between
799 photoactivated rhodopsin and its kinase: stability and kinetics of complex
800 formation. *Biochemistry* **32**, 14082-14088 (1993).
801 72. R. Paulsen, J. Bentrop, Activation of rhodopsin phosphorylation is triggered by
802 the lumirhodopsin-metarhodopsin I transition. *Nature* **302**, 417-419 (1983).
803 73. T. W. M. De Groof *et al.*, Selective targeting of ligand-dependent and -
804 independent signaling by GPCR conformation-specific anti-US28 intrabodies. *Nat*
805 *Commun* **12**, 4357 (2021).
806 74. J. S. Burg *et al.*, Structural biology. Structural basis for chemokine recognition
807 and activation of a viral G protein-coupled receptor. *Science* **347**, 1113-1117
808 (2015).
809 75. T. F. Miles *et al.*, Viral GPCR US28 can signal in response to chemokine
810 agonists of nearly unlimited structural degeneracy. *Elife* **7** (2018).
811 76. N. Tsutsumi *et al.*, Atypical structural snapshots of human cytomegalovirus
812 GPCR interactions with host G proteins. *Sci Adv* **8**, eabl5442 (2022).
813 77. C. T. Gilliland, C. L. Salanga, T. Kawamura, J. Trejo, T. M. Handel, The
814 chemokine receptor CCR1 is constitutively active, which leads to G protein-
815 independent, beta-arrestin-mediated internalization. *J Biol Chem* **288**, 32194-
816 32210 (2013).
817 78. M. Lefrancois *et al.*, Agonists for the Chemokine Receptor CXCR4. *ACS Med*
818 *Chem Lett* **2**, 597-602 (2011).
819 79. T. K. Ritchie *et al.*, Chapter 11 - Reconstitution of membrane proteins in
820 phospholipid bilayer nanodiscs. *Methods Enzymol* **464**, 211-231 (2009).
821 80. R. F. Pauszek, 3rd, R. Lamichhane, A. Rajkarnikar Singh, D. P. Millar, Single-
822 molecule view of coordination in a multi-functional DNA polymerase. *Elife* **10**
823 (2021).
824 81. R. Lamichhane, A. Solem, W. Black, D. Rueda, Single-molecule FRET of protein-
825 nucleic acid and protein-protein complexes: surface passivation and
826 immobilization. *Methods* **52**, 192-200 (2010).
827 82. L. R. Rabiner, A Tutorial on Hidden Markov-Models and Selected Applications in
828 Speech Recognition. *P Ieee* **77**, 257-286 (1989).
829 83. G. Schwarz, Estimating the Dimension of a Model. *Ann. Statist.* **6**, 461-464
830 (1978).
831 84. S. A. McKinney, C. Joo, T. Ha, Analysis of single-molecule FRET trajectories
832 using hidden Markov modeling. *Biophys J* **91**, 1941-1951 (2006).

Figures and Tables

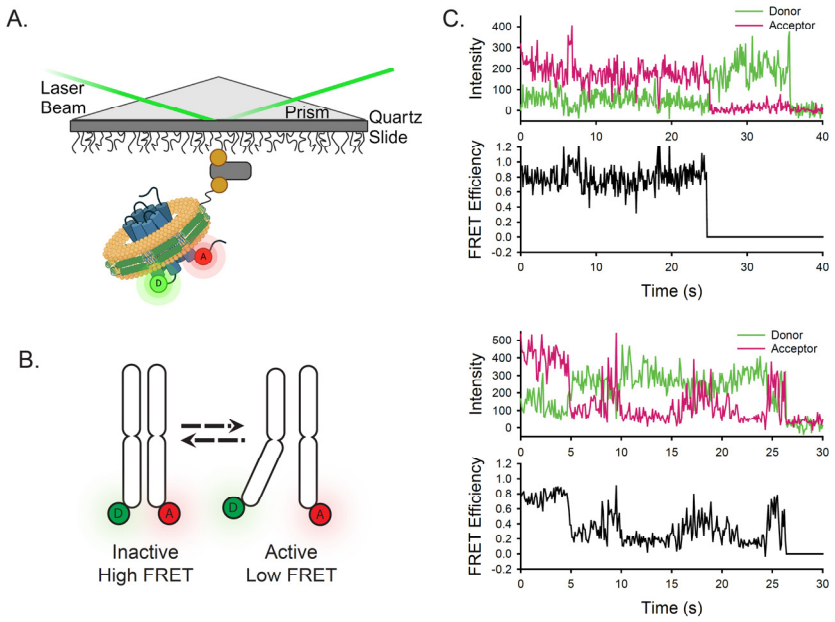

Figure 1. Experimental design of the smFRET system. A) A single receptor molecule (blue) was labeled with donor (D) and acceptor (A) fluorophores, inserted into a phospholipid (yellow) nanodisc (green), and immobilized on a quartz slide via biotin (brown circle)-neutravidin (grey rectangle) attachment. A prism facilitates total internal reflection of the excitation laser to excite only donor fluorophores close to the surface. B) Cartoon depicting inactive (left) and active (right) receptor conformations. C) Two representative single-molecule time traces for apo-ACKR3. In both examples, the donor (green) and acceptor (red) intensities are shown in the top panel and the corresponding FRET efficiency (black) is shown in the bottom panel.

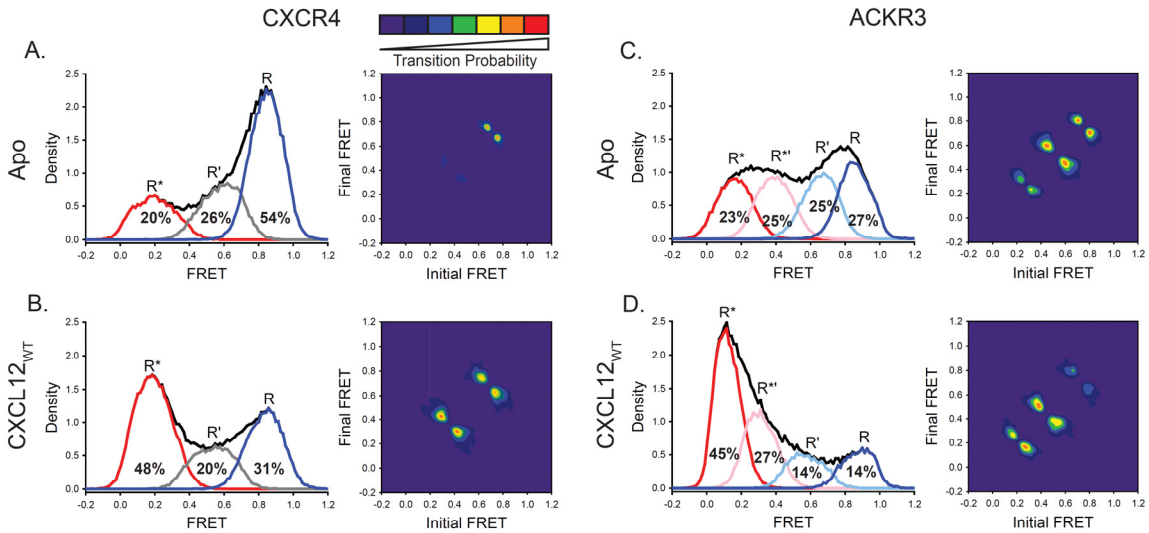

Figure 2. ACKR3 exhibits greater conformational flexibility compared to CXCR4. A) FRET efficiency histogram of apo-CXCR4 (left, black trace) resolved into three distinct conformational states: a high-FRET state corresponding to the inactive receptor conformation (R, blue), a low-FRET active receptor conformation (R*, red) and an intermediate conformation (R', gray). The fractional populations of each state obtained from global analysis are indicated. The receptor is mostly in the inactive conformation. A transition density probability (TDP) plot (right) displays the relative probabilities of transitions from an initial FRET state (x-axis) to a final FRET state (y-axis). For apo-CXCR4, transitions between R and R' states are observed most frequently. B) Addition of CXCL12 to CXCR4 shifted the conformational distribution to the low-FRET R* state and resulted in more transitions between all three FRET states. C) The broad FRET efficiency histogram of apo-ACKR3 (left, black trace) is resolved into four distinct conformational states: inactive R (blue), active R* (red), inactive-like R' (light blue), and active-like R*' (pink). Little conformational preference is observed among these states. Moreover, all possible sequential state-to-state transitions are observed (right). D) Addition of CXCL12 to ACKR3 shifted the conformational distribution to the low-FRET R* state, which was also reflected in the transition probabilities. In all cases, data sets represent the analysis of at least three independent experiments.

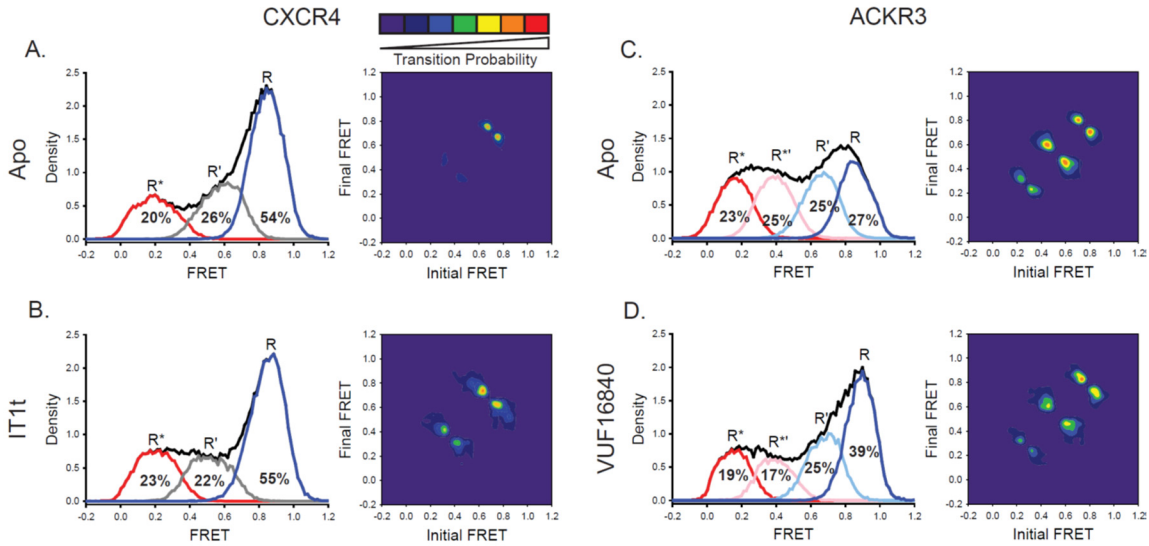

Figure 3. A small molecule inhibitor shifts the ACKR3 conformational population to the inactive FRET state, while CXCR4 is largely unaffected. A) FRET distributions and TDP of apo-CXCR4 repeated from Fig. 2A for comparison. B) Treatment of CXCR4 with the inhibitor IT1t had little impact on the FRET distribution (compared to 2A), but increased transition probabilities compared to the apo-receptor. C) FRET distributions and TDP of apo-ACKR3 repeated from Fig. 2C for comparison. D) Treatment of ACKR3 with VUF16480, an inverse agonist, shifted the conformational distribution and TDPs to the high-FRET inactive R conformation. Data sets represent the analysis of at least three independent experiments. The overall FRET efficiency envelopes for the samples are represented by the black traces.

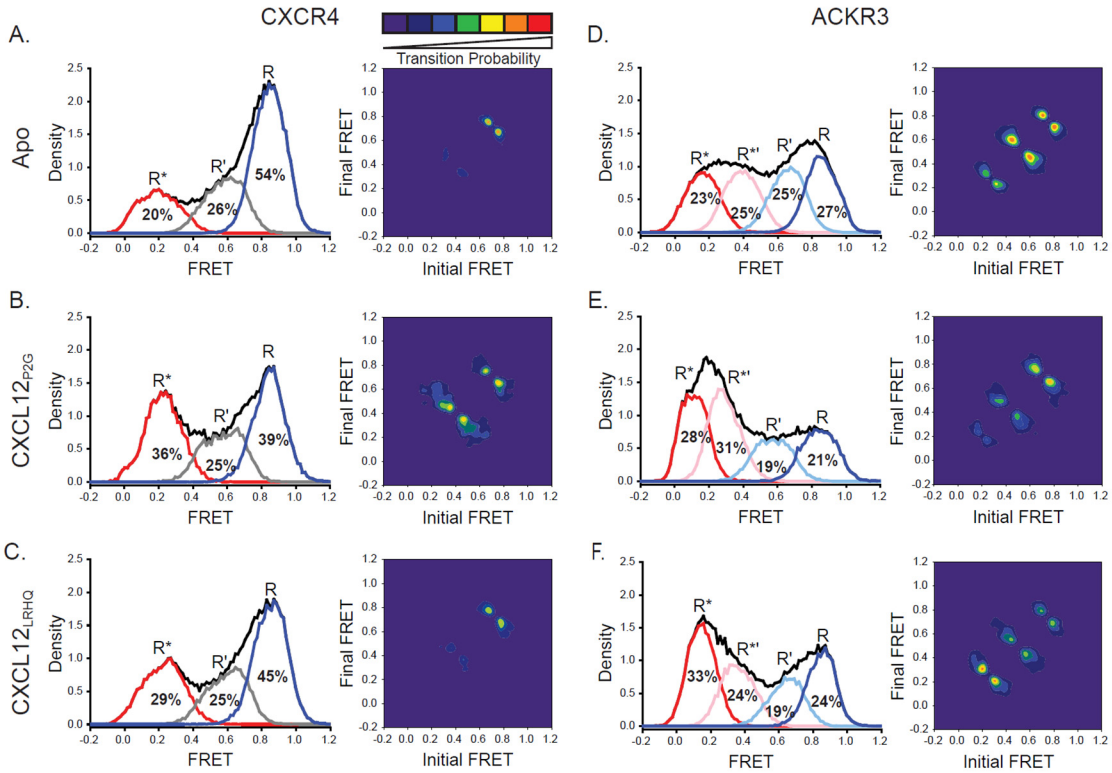

Figure 4. CXCL12 variants containing mutations to the N-terminus promoted active receptor conformations in both CXCR4 and ACKR3. A) FRET distributions and TDP for apo-CXCR4 repeated from Fig. 2A for reference. B) Addition of $CXCL12_{P2G}$ to CXCR4 promoted a shift to the low-FRET active (R*) conformation and an increase in state-to-state transition probabilities. C) $CXCL12_{LRHQ}$ led to a more subtle shift to the R* conformation of CXCR4 without affecting the transition probabilities. D) FRET distributions and TDPs for apo-ACKR3 repeated from Fig. 2C. E) Treatment of ACKR3 with $CXCL12_{P2G}$ displayed a shift to low-FRET, R*' and R* states, while reducing the transition probabilities for R' ↔ R*' and R*' ↔ R* transitions relative to the apo-receptor. F) $CXCL12_{LRHQ}$ treatment of ACKR3 shifted the FRET distribution to the low-FRET R* active state and promoted R*' ↔ R* transitions relative to the apo-receptor. In all cases, the data sets represent the analysis of at least three independent experiments. The overall FRET efficiency envelopes for the samples are represented by the black traces.

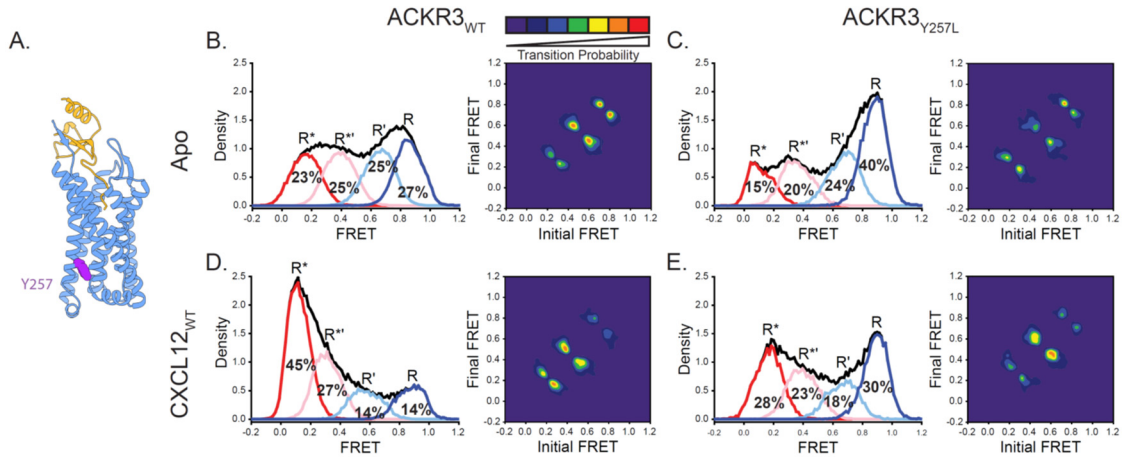

Figure 5. Replacement of Y257$^{6.40}$ with the corresponding residue in CXCR4 (leucine) reduces conformational heterogeneity of ACKR3. A) Structure of ACKR3 bound with CXCL12$_{WT}$ (PDBID: 7SK3) highlighting the location of Y257$^{6.40}$ (purple) (16). B) FRET efficiency distributions and TDP of WT ACKR3 in the apo-state, repeated from Fig. 2C. C) The mutation Y257$^{6.40}$L shifted the conformational landscape of the apo-receptor to the high-FRET inactive R conformation at the expense of active R* and active-like R*' conformations, and also reduced the probability of state-to-state transitions. D) FRET efficiency distributions and TDP of WT ACKR3 treated with CXCL12, repeated from Fig. 2D. E) Treatment of Y257$^{6.40}$L ACKR3 with CXCL12 promoted more low-FRET active R* and active-like R*' states. Data sets represent the analysis of at least three independent experiments. The overall FRET efficiency envelopes for the samples are represented by the black traces.

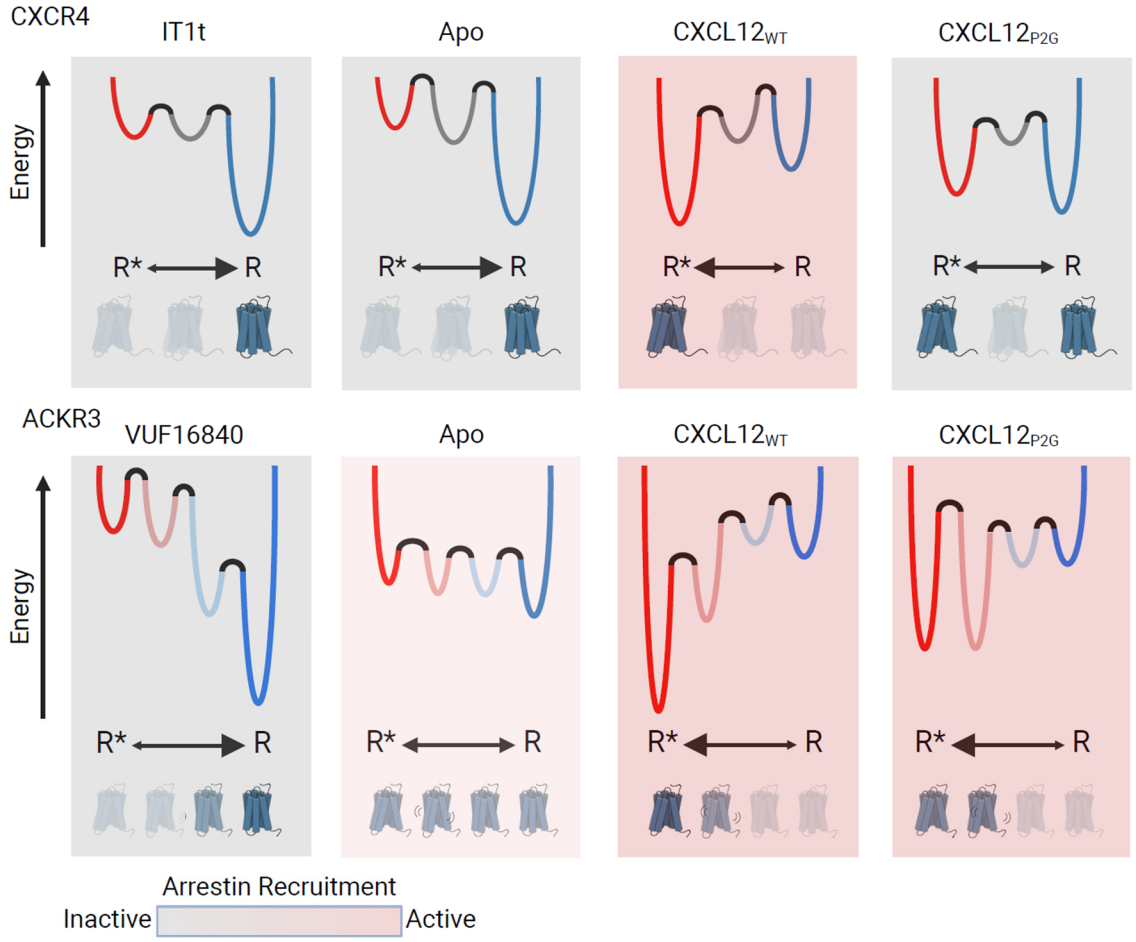

Figure 6. Schematic of the conformational energy landscapes for CXCR4 and ACKR3, highlighting the differences in the responsiveness of the two receptors to ligands. CXCR4 populates three distinct conformations, shown here as wells on the energy landscape. Apo-CXCR4 is predominantly in the inactive R state. The receptor is converted incompletely to R* with $CXCL12_{WT}$ treatment, while the antagonist IT1t has little impact on the conformational distribution. Though $CXCL12_{P2G}$ is an antagonist, the ligand promoted a detectable shift to the active R* state, suggesting TM6 movement is not sufficient for CXCR4 activation. In contrast, ACKR3 populates four distinct conformations and shows little preference among them in the apo-form. The inverse agonist, VUF16840, shifts the population to the inactive R conformation, while the agonists $CXCL12_{WT}$ and $CXCL12_{P2G}$ promote the R* and R*' populations of ACKR3. Despite stabilizing different levels of the active R* state and active-like intermediate R*' state, both $CXCL12_{WT}$ and $CXCL12_{P2G}$ are agonists of ACKR3. The flexibility of ACKR3 may contribute to the ligand-promiscuity of this atypical receptor. Figure created with biorender.com